Check for updates

Chemistry
Europe
European Chemical
Societies Publishing

Structural, Physical, Theoretical and Spectroscopic Investigations of Mixed-Valent Eu₂Ni₈Si₃ and Its Structural *Anti*-Type Sr₂Pt₃Al₈

Frank Stegemann,[a] Theresa Block,[a] Steffen Klenner,[a] Yuemei Zhang,[b, c]
Boniface P. T. Fokwa,[b] Carsten Doerenkamp,[d] Hellmut Eckert,[d, e] and Oliver Janka*[a, f]

Eu₂Ni₈Si₃ and its *anti*-type representative Sr₂Pt₃Al₈ were synthesized from the elements. They crystallize in the tetragonal crystal system with space group $P4_2/nmc$ and with lattice parameters of $a = 997.9(1)$ and $c = 747.6(1)$ pm (Eu₂Ni₈Si₃) as well as $a = 1082.9(2)$ and $c = 823.3(2)$ pm (Sr₂Pt₃Al₈). Both compounds were investigated via single crystal X-ray diffraction, indicating slight Si/Ni mixing for the silicide. Sr₂Pt₃Al₈ exhibits a temperature independent magnetic susceptibility, suggesting superimposed dia- and *Pauli*-paramagnetic contributions. The independent Al and Pt sites of the platinide were further characterized by ²⁷Al and ¹⁹⁵Pt solid-state NMR spectroscopy, which were assigned with the help of electronic structure calculations. ICOHP calculations and Bader charges were used to analyze the bonding situation. Eu₂Ni₈Si₃ in contrast is paramagnetic with a ferromagnetic transition at $T_C = 46.9(2)$ K and exhibits an effective magnetic moment of $\mu_{eff} = 6.61(1)$ μB per Eu atom. The latter is in line with an intermediate valence that was further proven by ¹⁵¹Eu Mößbauer spectroscopic investigations. At 300 K, the refined Eu²⁺/Eu³⁺ ratios are 60%/40%, at 78 K 62% and 38% (Eu²⁺/Eu³⁺) are observed, being in line with the ratio deduced from the magnetic susceptibility. Finally, at 6 K a ratio of 68% Eu²⁺ and 32% Eu³⁺ was observed. Below the *Curie* temperature, the Eu²⁺ signal shows a full magnetic hyperfine splitting, with an internal magnetic field value of $B_0 = 28.4$ T.

1. Introduction

In the Pearson database[1] only a limited number of intermetallic alkaline earth compounds of the general formula $EA_xT_yAl_z$ with

[a] Dr. F. Stegemann, Dr. T. Block, S. Klenner, Dr. O. Janka
Institut für Anorganische und Analytische Chemie,
Westfälische Wilhelms-Universität Münster,
Corrensstraße 30, 48149 Münster, Germany
[b] Prof. Dr. Y. Zhang, Prof. Dr. B. P. T. Fokwa
Department of Chemistry,
University of California,
501 Box Springs Rd, Riverside, CA, 92521, USA
[c] Prof. Dr. Y. Zhang
Department of Chemistry and Physics,
Warren Wilson College,
Asheville, NC, 28815, USA
[d] Dr. C. Doerenkamp, Prof. Dr. H. Eckert
Instituto de Física de São Carlos,
Universidade de São Paulo,
São Carlos – SP, 13566-590, Brazil
[e] Prof. Dr. H. Eckert
Institut für Physikalische Chemie,
Westfälische Wilhelms-Universität Münster,
Corrensstraße 28, 48149 Münster, Germany
[f] Dr. O. Janka
Saarland University, Inorganic Solid-State Chemistry,
Campus, Building C4 1, 66123 Saarbrücken, Germany
E-mail: oliver.janka@uni-saarland.de
https://www.uni-saarland.de/lehrstuhl/kickelbick/kickelbick-mitarbeiter/dr-oliver-janka.html

the constituent elements $EA = $ Ca, Sr, Ba and $T = $ Pd, Pt, and Au are known. For calcium, CaPdAl[2] (own type), Ca₂T₂Al[3] ($T = $ Pd, Pt; Ca₂Ir₂Si type[4]), CaPd₃Al₅[5] (own type), CaPtAl[6] (*anti*-TiNiSi type[7]), CaAuAl[2b] (TiNiSi type[7]), CaAu₁₋ₓAl₃₊ₓ[8] ($x = 0.1$, 0.2; ThCr₂Si₂ type[9]), the icosahedral quasicrystal CaAu₄.₅₋ₓAl₁.₅₊ₓ as well as the 1/0 crystalline approximant CaAu₃₊ₓAl₁₋ₓ[10] and CaAu₃Al₇[11] (ScRh₃Si₇ type[12]) are described. For the heavier homologue strontium, SrAuAl₃[13] (ThCr₂Si₂ type[9]), several members of the solid solution SrAu₄₊ₓAl₃₋ₓ[14] (Ba₃Ag₁₄.₆Al₆.₄ type[15]), SrAu₅.₀₅Al₁.₉₅[14] (BaAu₅Ge₂ type[16]), Sr₂Au₆₊ₓAl₃₋ₓ[17] (Sr₂Au₆Zn₃ type[18]), SrAu₂₋ₓAl₂₊ₓ[19] (CaBe₂Ge₂ type[20]), SrAu₃Al₂[21] (RbAu₃Al₂ type[22]), and SrAu₂.₈₃Al₂.₁₇[21] (BaZn₅ type[23]) have been reported. For barium finally, Ba₃Pt₄Al₄[24] (own type), BaAu₂.₈₉Al₂.₁₁[21] (BaZn₅ type[23]), and two members of the solid solution BaAu₇₋ₓAl₆₊ₓ[21,25] (NaZn₁₃ type[26]) are listed. In the past few years we have started to investigate the ternary $EA-T-$Al ($EA = $ Ca, Sr, Ba; $T = $ Pd, Pt, Au) systems ourselves in more detail and extended the knowledge of the few known compounds. Several compounds were synthesized and structurally characterized, e.g. Ca₂Pt₆Al₁₅[27] (Sc₂Pt₆Al₁₅ type[27]), CaPtAl₂[28] (MgCuAl₂ type[29]), CaAu₂Al₂[19b] (*anti*-ThRu₂P₂ type[30]), Sr₂Pd₂Al[31] (Ca₂Pd₂Ge type[3]), Sr₂Pd₄Al₅[32] (own type), the incommensurately (3 + 2)D modulated SrPt₂Al₂[33] (CaBe₂Ge₂ type[20]), SrPt₃Al₂[31] (CeCo₃B₂ type[34]), SrPtAl₂[28] (MgCuAl₂ type[29]) or BaPtAl₂[28] (MgCuAl₂ type[29]), BaAuAl[35] (LaIrSi type[36]) and Ba₃Au₅₊ₓAl₆₋ₓ[19b] (own type). All of these compounds exhibit $[T_xAl_y]^{\delta-}$ polyanionic networks with the alkaline earth metals occupying voids. Theoretical as well as X-ray photoelectron spectroscopic investigations (XPS) on those compounds revealed negatively charged transition metals in line with the corresponding

electronegativities[37] and electron affinities[37] and therefore an electron transfer from the alkaline earth metals onto the polyanions. For the ternary $RE–T–Al$ (RE = rare earth element; T = Pd, Pt, Au) systems, in contrast, around 270 entries are listed in the Pearson database.[1] When looking at nickel as a lighter homologue of Pd and Pt, the hexagonal intermetallic $EANi_2Al_9$[38] compounds (EA = Ca, Sr, Ba; $BaFe_2Al_9$ type[38]) were reported. Moreover, for EA = Ca and T = Ni, $CaNiAl_9$ (own type)[39] and $CaNi_2Al_8$ ($CeFe_2Al_8$ type[40])[41] are described. The only EA rich compounds with T = Ni can be found in the triclinic pseudoternary system $Ca_8(Ni_xAl_{1-x})_3$ (x = 0.1–0.4; Ca_8In_3 type[42]).[43]

We have continued our endeavors in the ternary Sr–Pt–Al system and initially found tetragonal $Sr_2Pt_3Al_8$ ($anti$-$Eu_2Ni_8Si_3$ type) as a side product during attempts to synthesize $SrPtAl_2$.[28] The compound was subsequently synthesized as phase-pure material and characterized by powder and single crystal X-ray diffraction experiments, ^{27}Al and ^{195}Pt solid-state NMR spectroscopy and first-principles electronic structure calculations. Since aristotypic $Eu_2Ni_8Si_3$ was reported to have an intermediate Eu-valence of $+2.38$, which was only investigated by XANES measurements so far,[44] we decided to resynthesize the compound and characterize it by single crystal X-ray diffraction, magnetic measurements and ^{151}Eu Mößbauer spectroscopy.

2. Results and discussion

2.1. Structure refinement

A careful analysis of the obtained data set of $Sr_2Pt_3Al_8$ revealed a primitive tetragonal lattice and the centrosymmetric space group $P4_2/nmc$ was found to be correct during structure refinement. The starting values of the atomic parameters were first obtained from the Superflip algorithm.[45] The structure was refined using a least-squares algorithm (F^2) implemented in the JANA2006 software package.[46] All atomic sites were refined using anisotropic displacements in a first step. As a check for correct composition, the occupancy factors of all atomic sites were refined in separate series of least-squares cycles. All sites were fully occupied within three standard deviations.

Due to the results of the magnetic measurements and the ^{151}Eu Mößbauer spectroscopic investigations, indicating an intermediate Eu valence state for $Eu_2Ni_8Si_3$, a single crystal from an annealed sample was investigated. The starting values of the atomic parameters were taken from the literature.[44] All atomic sites were refined using anisotropic displacements. During the check for correct composition, the Ni3 site showed a reduced occupancy, which was compensated by a mixed occupation with Si, and a ratio of Ni:Si = 91(1):9(1) was refined. All other sites were fully occupied within three standard deviations, resulting in a final composition of $Eu_2Ni_{7.82(2)}Si_{3.18(2)}$. For simplicity, an idealized sum formula $Eu_2Ni_8Si_3$ will be used for further description. For both, the Ni3/Si3 and the single Eu site, slightly enhanced U_{33} displacement parameters were observed, which, in combination with the experimentally observed Eu^{2+}/Eu^{3+} ratio, lead us to address a potential superstructure formation. The only direct possibility is to split the Eu site in a 2:1 (close to

the experimentally observed) ratio by an $isomorphic$ symmetry reduction of index 3, leading to a tripling of the c axis. However, neither in the single crystal nor in the powder diffraction experiments, superstructure reflections were observed. $Translationengleiche$ symmetry reductions of index 2, leading to the space groups $P\bar{4}c2$, $P4_22_12$ and $Cmme$ were also tested, with no success. In addition, the NMR results obtained on the isostructural Sr compound show no evidence of superstructure formation.

Final difference Fourier-syntheses were contour less in both cases. Details of the refinement as well as atomic coordinates, anisotropic displacement parameters and interatomic distances can be found in Tables 1–4.

2.2. Crystal Chemistry

$Sr_2Pt_3Al_8$ crystallizes in the tetragonal crystal system with centrosymmetric space group $P4_2/nmc$ and unit cell dimensions of a = 1082.9(2) and c = 823.3(2) pm ($Wyckoff$-sequence hg^3fd). A check with the Pearson database[1] revealed isotypism with the $Eu_2Ni_8Si_3$ type structure[44] with the Pt atoms occupying the two crystallographically independent Si sites and the Al atoms occupying the three independent Ni sites, respectively. The formation of $antitypic$ aluminum compounds in comparison to the ternary nickel silicides has also been observed e.g. in equiatomic $CaPtAl$[6] ($anti$-TiNiSi type[7]), orthorhombic $CePt_2Al_5$[47] ($anti$-YNi_5Si_3 type[48]) or the $anti$-$Gd_3Ru_4Al_{12}$ type[49] silicides $RE_3Ni_{12}Si_4$ (RE = Y, Gd–Tm).[50]

Since $Sr_2Pt_3Al_8$ represents a new intermetallic compound, its crystal structure will be described exemplarily. The structure is best described by $(Al_4)_5$ supertetrahedral units consisting of a central $(Al3)_4$ tetrahedron whose corners are connected to four other aluminum tetrahedra (Figure 1). However, it should be noted, that homoatomic Al–Al bonds are weaker in comparison to heteroatomic Pt–Al contacts ($vide\ infra$). The interatomic Al–Al distances within those units range between 267 and 284 pm which is shorter than in fcc Al (286 pm)[51] but above the sum of covalent radii ($2 \times 125 = 250$ pm).[37] These distances are comparable to those found in other ternary aluminum rich platinides as the 3D monoclinic approximant of $Eu_2Pt_6Al_{15}$ (263–298 pm)[52] and $Ce_2Pt_6Al_{19}$ (273–315 pm)[53] or in binary Pt_8Al_{21} (262–300 pm).[54]
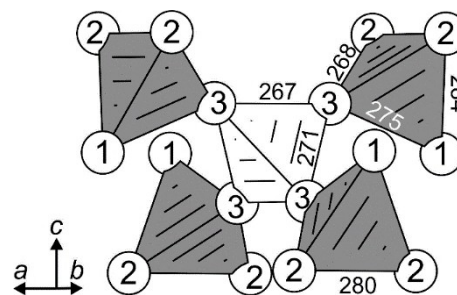

Figure 1. $(Al_4)_5$ supertetrahedra in $Sr_2Pt_3Al_8$. Interatomic distances are given in pm.

EurJIC
European Journal of Inorganic Chemistry

Full Papers
doi.org/10.1002/ejic.202100564

Chemistry Europe
European Chemical
Societies Publishing

Table 1. Crystal data and structure refinement of $Sr_2Pt_3Al_8$ (anti-$Eu_2Ni_8Si_3$ type, space group $P4_2/nmc$, $Z=4$) and $Eu_2Ni_{7.82(2)}Si_{3.18(2)}$ ($Eu_2Ni_8Si_3$ type, space group $P4_2/nmc$, $Z=4$) refined from the single crystal X-ray diffraction experiment.

Refined composition		$Sr_2Pt_3Al_8$	$Eu_2Ni_{7.82(2)}Si_{3.18(2)}$
Formula weight, $g\,mol^{-1}$		976.3	852.2
Crystal size, μm^3		$200\times50\times33$	$110\times60\times25$
Diffractometer type		Stoe IPDS-II	Stoe IPDS-II
Wave length, pm		71.073 (Mo$K\alpha$)	71.073 (Mo$K\alpha$)
Unit cell dimensions			
a/pm		1083.32(5)	997.12(5)
c/pm		823.28(3)	746.77(4)
V/nm³		0.9662	0.7425
Calculated density, $g\,cm^{-3}$		6.71	7.67
Transmission ratio (min/max)		0.028/0.293	0.072/0.344
Detector distance, mm		70	70
Exposure time, min		5	7
Integr. param. ($A/B/EMS$)		14.0/−1.0/0.030	14.0/−1.0/0.030
Absorption correction		numerical	numerical
Absorption coefficient, mm^{-1}		54.9	36.4
$F(000)$, e		1656	1558
θ range for data collection, deg		2.7–33.4	2.9–33.3
Range in hkl		±16; -14, $+16$; -12, $+10$	±13; ±15; ±11
Total no. of reflections		13069	8658
Independent reflections/R_{int}		1024/0.0403	795/0.0813
Reflections with $I>3\,\sigma(I)/R_\sigma$		733/0.0137	559/0.0307
Data/parameters		1024/38	795/39
Goodness-of-fit		0.99	0.98
Final R indices [$I>3\,\sigma(I)$]	$R=$	0.0153	0.0196
	w$R=$	0.0314	0.0383
R indices for all data	$R=$	0.0298	0.0417
	w$R=$	0.0344	0.0426
Extinction scheme		Lorentzian isotropic [64]	Lorentzian isotropic [64]
Extinction coefficient		1520(30)	460(30)
Largest diff. peak		$+1.43$	$+1.45$
and hole, $e\,Å^{-3}$		-1.53	-1.25

Table 2. Atomic positions and equivalent isotropic displacement parameters (pm²) of $Sr_2Pt_3Al_8$ (anti-$Eu_2Ni_8Si_3$ type, space group $P4_2/nmc$, $Z=4$) and $Eu_2Ni_{7.82(2)}Si_{3.18(2)}$ ($Eu_2Ni_8Si_3$ type, space group $P4_2/nmc$, $Z=4$), refined from the single crystal X-ray diffraction experiment. U_{eq} is defined as one third of the trace of the orthogonal U_{ij} tensor.

Atom	Wyckoff site	x	y	z	U_{eq}
$Sr_2Pt_3Al_8$					
Sr	8g	1/4	0.54586(5)	0.88595(7)	128(2)
Pt1	4d	1/4	1/4	0.00304(4)	99(1)
Pt2	8f	0.45549(1)	$-x$	1/4	100(1)
Al1	8g	1/4	0.11033(15)	0.2488(2)	125(4)
Al2	16h	0.04188(11)	0.12083(11)	0.03531(15)	114(3)
Al3	8g	1/4	0.62665(15)	0.3681(2)	107(4)
$Eu_2Ni_{7.82(2)}Si_{3.18(2)}$					
Eu	8g	1/4	0.54549(3)	0.89170(5)	124(1)
Ni1	8g	1/4	0.11310(9)	0.25787(11)	102(4)
Ni2	16h	0.04305(6)	0.12304(6)	0.03266(8)	99(1)
Ni3/Si3[a]	8g	1/4	0.62231(9)	0.35324(13)	119(3)
Si1	4d	1/4	1/4	0.00304(4)	89(6)
Si2	8f	0.45775(13)	$-x$	1/4	100(3)

[a] Refined Ni3 to Si3 ratio is 0.91(1) to 0.09(1).

In Figure 2, the crystal structure of $Sr_2Pt_3Al_8$ is depicted along the b-axis, focusing on the supertetrahedral units and empty distorted Sr_4 tetrahedra, which occupy the remaining voids. The structural units reveal an AB stacking sequence along the c direction according to the 4_2 screw axis. Both substructures, however, are arranged in a distorted bcc arrangement at the same time and might therefore be described as hierarchical derivatives of tungsten.[55] The Sr atoms are surrounded according to $Sr@Al_{11}Pt_5+Sr_2$ (CN $=16+2$; Figure 3). The interatomic Sr–Al distances (314–372 pm) are significantly shorter than those found in binary Sr_xAl_y compounds such as $SrAl_4$ (342 pm)[56] or KHg_2 type[57] $SrAl_2$ (330–359 pm)[58] but are in the range of the sum of the covalent radii[37] (317 pm) and those found in $SrPt_2Al_2$ (average 334–368 pm)[33] indicating a covalent bonding character. The Sr–Pt distances of 335–373 pm are in the range of other binary Sr_xPt_y compounds as $SrPt_2$ (321 pm)[59] and $SrPt_5$ (311+347 pm)[59] or ternary $SrPt_2Al_2$ (330–388 pm).[33] The interatomic Sr–Sr distances of 385 pm are significantly shorter than in fcc Sr (426 pm)[60] but equal to the sum of the covalent radii (384 pm).[37] Due to an electron transfer from the

EurJIC
European Journal of Inorganic Chemistry

Full Papers
doi.org/10.1002/ejic.202100564

Chemistry
Europe
European Chemical
Societies Publishing

Table 3. Anisotropic displacement parameters (pm^2) of Sr$_2$Pt$_3$Al$_8$ (*anti*-Eu$_2$Ni$_8$Si$_3$ type, space group $P4_2/nmc$, $Z=4$) and Eu$_2$Ni$_{7.82(2)}$Si$_{3.18(2)}$ (Eu$_2$Ni$_8$Si$_3$ type, space group $P4_2/nmc$, $Z=4$), refined from the single crystal X-ray diffraction experiment.

Atom	*Wyckoff* site	U_{11}	U_{22}	U_{33}	U_{12}	U_{13}	U_{23}
Sr$_2$Pt$_3$Al$_8$							
Sr	8g	108(2)	136(2)	139(2)	0	0	5(2)
Pt1	4d	94(2)	100(2)	103(1)	0	0	0
Pt2	8f	98(1)	U_{11}	105(1)	6(5)	0(1)	U_{13}
Al1	8g	137(6)	117(6)	121(6)	0	0	14(8)
Al2	16h	118(5)	102(4)	123(5)	−10(4)	−6(4)	4(4)
Al3	8g	95(6)	75(6)	150(7)	0	0	7(6)
Eu$_2$Ni$_{7.82(2)}$Si$_{3.18(2)}$							
Eu	8g	90(2)	132(2)	150(1)	0	0	29(1)
Ni1	8g	116(4)	102(4)	88(3)	0	0	19(3)
Ni2	16h	105(2)	87(2)	106(2)	−5(2)	0(2)	10(2)
Ni3/Si3	8g	94(4)	89(4)	172(5)	0	0	3(3)
Si1	4d	98(11)	71(10)	98(10)	0	0	0
Si2	8f	103(4)	U_{11}	92(7)	5(6)	2(4)	U_{13}

Table 4. Interatomic distances (in pm) of Sr$_2$Pt$_3$Al$_8$ (*anti*-Eu$_2$Ni$_8$Si$_3$ type, space group $P4_2/nmc$, $Z=4$) and Eu$_2$Ni$_{7.82(2)}$Si$_{3.18(2)}$ (Eu$_2$Ni$_8$Si$_3$ type, space group $P4_2/nmc$, $Z=4$), refined from the single crystal X-ray diffraction experiment. Standard deviations are smaller or equal to ±0.3 pm; all distances of the first coordination sphere are given.

Sr$_2$Pt$_3$Al$_8$								Eu$_2$Ni$_{7.82(2)}$Si$_{3.18(2)}$							
Sr	2	Al2	314.0	Al1	1	Pt1	252.6	Eu	2	Ni2	286.2	Ni1	1	Si1	226.3
	2	Al3	328.3		1	Pt1	258.3		2	Ni3/Si3	306.7		1	Si1	236.3
	2	Al2	332.8		1	Al3	274.9		2	Ni2	307.5		1	Ni3/Si3	245.3
	2	Al2	334.5		2	Pt2	278.7		1	Si1	309.0		2	Ni2	251.0
	1	Pt1	334.7		2	Al2	284.1		2	Ni2	309.4		2	Si2	258.7
	1	Al1	343.3		2	Al2	286.1		1	Ni1	315.9		2	Ni2	266.4
	2	Pt2	352.0		1	Al1	302.6		2	Si2	322.1		1	Ni1	273.0
	2	Al1	372.0		1	Sr	343.3		2	Si2	338.4		1	Eu	315.9
	2	Pt2	373.3		2	Sr	371.9		2	Ni1	339.8		2	Eu	339.8
	2	Sr	384.6	Al2	1	Pt2	251.6		1	Ni3/Si3	353.0	Ni2	1	Si2	231.3
Pt1	2	Al1	252.6		1	Pt2	266.0		2	Eu	357.7		1	Si2	241.4
	2	Al1	258.2		1	Pt1	266.7	Si1	2	Ni1	226.3		1	Si1	242.4
	4	Al2	266.6		1	Al3	268.1		2	Ni1	236.3		1	Ni3/Si3	247.4
	2	Sr	334.6		1	Al2	279.9		4	Ni2	242.4		1	Ni1	251.0
Pt2	2	Al2	251.7		1	Al2	283.1		2	Eu	309.0		1	Ni2	253.2
	2	Al3	258.7		1	Al1	284.1		2	Si1	373.4		1	Ni2	264.5
	2	Al2	266.0		1	Al1	286.1	Si2	2	Ni2	231.3		1	Ni1	266.4
	2	Al1	278.7		1	Sr	313.9		2	Ni3/Si3	235.0		1	Eu	286.2
	2	Sr	352.0		1	Sr	332.9		2	Ni2	241.4		1	Eu	307.5
	2	Sr	373.3		1	Sr	334.6		2	Ni1	258.7		1	Eu	309.4
				Al3	2	Pt2	258.7		2	Eu	322.1	Ni3/Si3	2	Si2	235.0
					1	Al3	267.3		2	Eu	338.4		2	Ni3/Si3	237.1
					2	Al2	268.0						1	Ni1	245.3
					2	Al3	271.2						2	Ni2	247.4
					1	Al1	274.9						1	Ni3/Si3	254.7
					2	Sr	328.3						2	Eu	306.7

Sr atoms onto the [Pt$_3$Al$_8$]$^{\delta-}$ polyanion, the Sr atoms exhibit a cationic character. This behavior has been observed in all alkaline earth aluminum transition metallides and is accompanied with a reduction of the radius of the Sr atoms. Subsequently, shorter Sr–Sr distances (here 385 pm) compared to the ones found in elemental Sr are observed.

Figure 4, finally, shows the crystal structure of tetragonal Sr$_2$Pt$_3$Al$_8$ along the *c* axis. As described before, the super-tetrahedral aluminum units are found in a distorted *bcc* arrangement with the remaining voids filled by Sr$_4$ tetrahedra and Pt atoms, respectively. The Pt substructure in turn is reminiscent of the atomic arrangement of binary CuAl$_2$[61] with both, Cu and Al, replaced by the transition metal. The two crystallographically independent Pt sites are surrounded by eight aluminum atoms *via* capping the faces, edges, and corners of the Al$_4$ tetrahedra with an additional capping of two (Pt1) and four (Pt4) Sr atoms, respectively (Figure 3). The heteroatomic distances of Pt and Al atoms are found between 252 and 279 pm. They are in the range of the sum of covalent radii (125 + 129 = 254 pm)[37] and suggest a covalent bonding character. Other alkaline earth aluminum platinides such as Ba$_3$Pt$_4$Al$_4$,[24] Ca$_2$Pt$_2$Al[3] or the orthorhombic 3 + 2D incommensurately modulated SrPt$_2$Al$_2$[33] show comparable distances (average: 249–255 pm). In Eu$_2$Ni$_8$Si$_3$, the Ni atoms occupy the Al positions and the Si atoms occupy the Pt sites. The interatomic distances (Table 4) are all in the typical range for intermetallic silicides and in good agreements with literature data.[44]
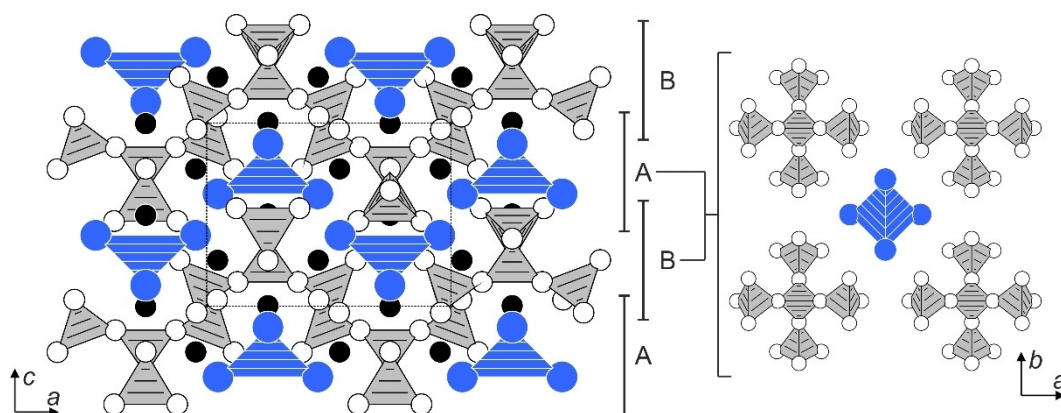
EurJIC
European Journal of Inorganic Chemistry

Full Papers
doi.org/10.1002/ejic.202100564

**Chemistry
Europe**
European Chemical
Societies Publishing

Figure 2. Unit cell of $Sr_2Pt_3Al_8$ along the crystallographic b axis (*left*) and both layers in the *ab* plane (*right*). Sr, Pt, and Al atoms are depicted as blue, black and open white circles. The Al supertetrahedral units and distorted Sr_4 tetrahedra are shown on the right.
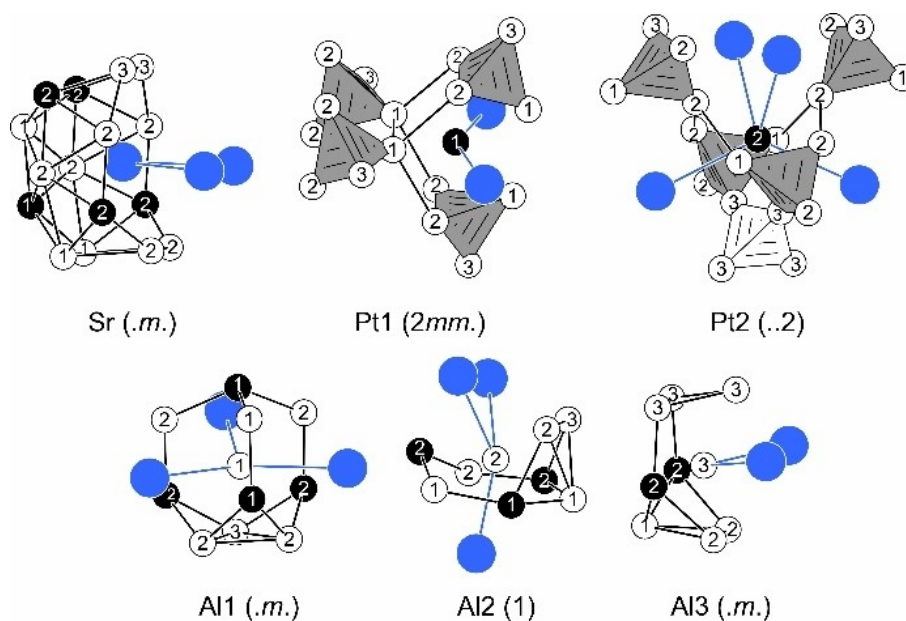

Figure 3. Coordination environments of the crystallographically independent sites in $Sr_2Pt_3Al_8$ with additional point symmetries given. Sr, Pt and Al atoms are depicted as blue, black and open white circles, respectively.

2.3. Physical Properties

The magnetic properties of $Sr_2Pt_3Al_8$ are depicted in Figure 5, the ones of $Eu_2Ni_8Si_3$ in Figure 6. The magnetic susceptibility of $Sr_2Pt_3Al_8$ is nearly temperature independent with an upturn below 75 K caused by paramagnetic impurities. The negative value $(\chi(300\,K) = -5.0(5) \times 10^{-5}\,emu\,mol^{-1})$ suggests that the *Pauli*-paramagnetism is overcompensated by the intrinsic core diamagnetism. The magnetic susceptibility of $Eu_2Ni_8Si_3$ is dominated by *Curie*-paramagnetism above 50 K. The inverse magnetic susceptibility (χ^{-1} data, Figure 6, top left) was fitted using the modified Curie-Weiss-law in the temperature region of $T = 150$–300 K and yielded an effective magnetic moment of $\mu_{eff} = 6.61(1)\,\mu_B$ per Eu atom. This is significantly below the theoretical value of $\mu_{calc} = 7.94\,\mu_B$ for a free Eu^{2+} ion[62] but

greatly above the typical experimental value for a free Eu^{3+} cation ($\mu_{calc,exp} = 3.5\,\mu_B$[62]). The temperature independent term was determined to be $\chi_0 = -5.8(1) \times 10^{-4}\,emu\,mol^{-1}$; the positive Weiss temperature of $\theta_P = 57.0(2)$ K suggests ferromagnetic interactions in the paramagnetic region. Additionally, low-field ZFC/FC experiments were performed at 100 Oe (Figure 6, top right) which revealed ferromagnetic ordering with a Curie-temperature of $T_C = 46.9(2)$ K, determined at the inflection point of the FC curve (Figure 6 top right, inset). Trace amounts of $Eu^{II}O$, which is a ferromagnet below $T_C = 77$ K,[63] cause the apparent phase transition at $T \sim 75$ K. The ferromagnetic ordering of the main phase results in a λ-shaped temperature dependence of the heat capacity (Figure 6 bottom left). The determined maximum of $T_{hc} = 45.2(2)$ K is in accordance with the ZFC/FC experiments. The bottom right panel of Figure 6,

EurJIC
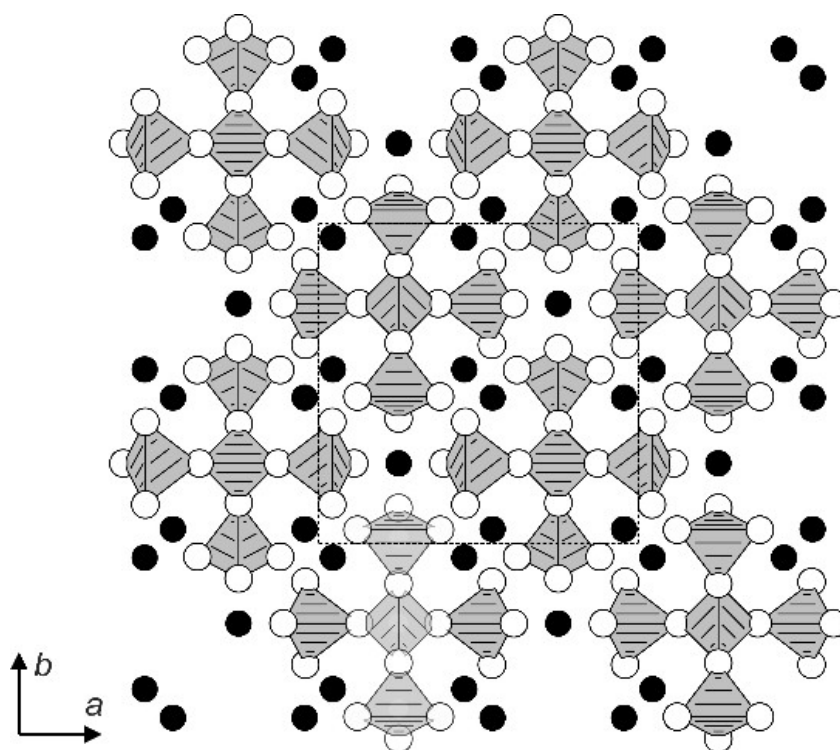European Journal of Inorganic Chemistry

Full Papers
doi.org/10.1002/ejic.202100564

Chemistry
Europe
European Chemical
Societies Publishing

Figure 4. Enlarged unit cell of $Sr_2Pt_3Al_8$ along the crystallographic *c* axis, highlighting the Al supertetrahedral units. Pt and Al atoms are depicted as black and white circles, respectively.
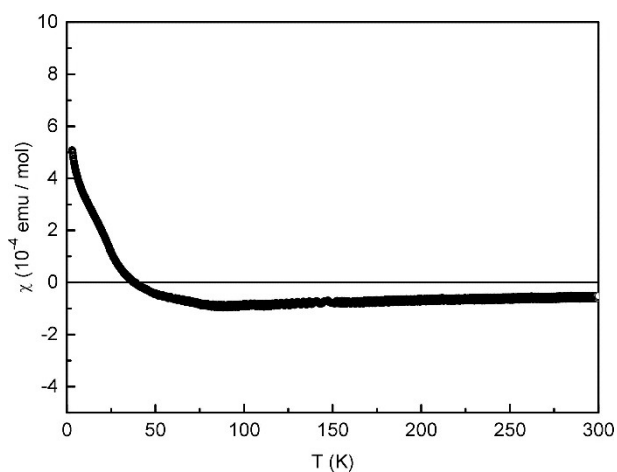

Figure 5. Temperature dependence of the magnetic susceptibility χ of $Sr_2Pt_3Al_8$ measured in zero-field-cooled (ZFC) mode at 10 kOe.

finally depicts the magnetization isotherms recorded at 3, 10 and 100 K. The isotherms at 3 and 10 K, thus below the Curie temperature T_C, confirm the ferromagnetic ground state and reveal the expected saturation behavior. The saturation magnetization, however, only reaches $\mu_{sat} = 4.17(1)$ μ_B per Eu atom at 3 K and 80 kOe. Again, this value is significantly below the theoretical value of $\mu_{sat,calc} = 7$ μ_B according to $g_J \times J$. The experimentally observed reduced magnetic moment and significantly reduced saturation magnetization suggest, due to the X-ray purity of the sample and the literature information, an

intermediate-valent state of the Eu atoms in $Eu_2Ni_8Si_3$. To calculate the relative ratios of Eu^{2+} vs. Eu^{3+} present, the following equation was used:

$$\mu_{eff,exp} = \sqrt{(1-x) \cdot \mu_{eff}^2(Eu^{2+}) + x \cdot \mu_{eff}^2(Eu^{3+})}.$$

For the effective magnetic moments, $\mu_{eff}(Eu^{2+}) = 7.94$ μ_B and $\mu_{eff}(Eu^{3+}) = 3.5$ μ_B were chosen. Solving the equation using the experimentally derived moment of $\mu_{eff,exp} = 6.61$ μ_B leads to $x = 0.38$, equal to 38% Eu^{3+}. Hence, the Eu atoms in $Eu_2Ni_8Si_3$ exhibit an intermediate oxidation state of $+2.38$. This is in perfect agreement with the Eu L_{III}-edge X-ray absorption near edge structure (XANES) spectroscopic data reported in the literature.[44] Bedan and co-workers deduced an intermediate valence of $+2.38$ per Eu atom as well, determined from the relative ratio of the maximum absorptions of the Eu^{2+} and Eu^{3+} signals. The intermediate valence in $Eu_2Ni_8Si_3$ is quite surprising, as only one crystallographically independent Eu site (Wyckoff site 8*g*) is present. Hence, instead of a valence ordering of the Eu^{2+} and Eu^{3+} cations one expects a dynamic fluctuation of the valence state. Our own single crystal diffraction experiments (*vide supra*) did not reveal any additional reflections that could be attributed to a superstructure formation. Further insights on the Eu valence state in $Eu_2Ni_8Si_3$ were obtained by ^{151}Eu Mößbauer spectroscopy (*vide infra*).

EurJIC
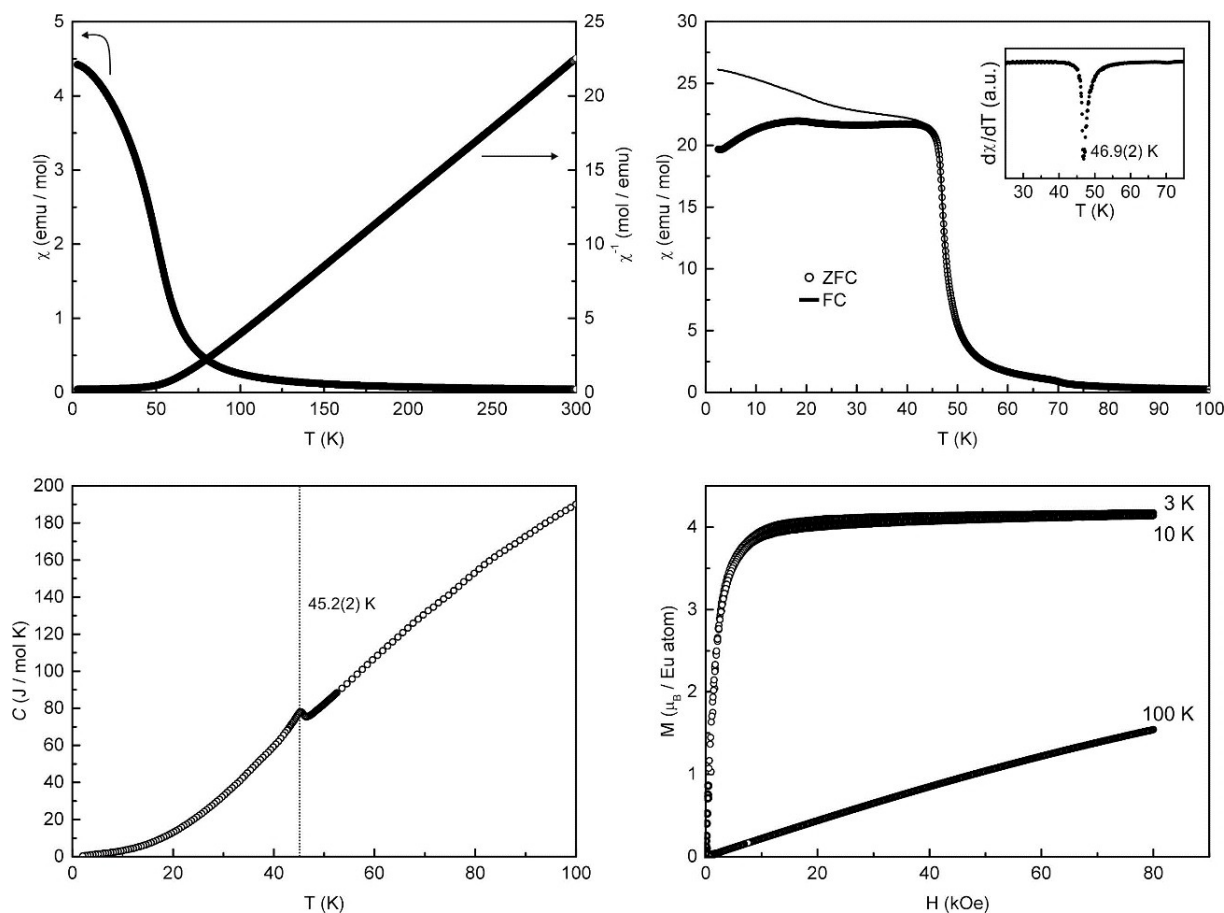European Journal of Inorganic Chemistry

Full Papers
doi.org/10.1002/ejic.202100564

Chemistry
Europe
European Chemical
Societies Publishing

Figure 6. Magnetic properties of $Eu_2Ni_8Si_3$: (*top left*) temperature dependence of the magnetic susceptibility χ and its reciprocal χ^{-1} measured at an applied external field of 10 kOe; (*top right*) magnetic susceptibility in zero-field-cooled (ZFC) and field-cooled (FC) mode at 100 Oe, the inset depicts the derivative $d\chi/dT$; (*bottom left*) temperature dependence of the specific heat capacity; (*bottom right*) magnetization isotherms, recorded at 3, 10, and 100 K.

2.4. ^{151}Eu Mößbauer Spectroscopy

The ^{151}Eu Mößbauer spectra of $Eu_2Ni_8Si_3$, measured at 300, 78 and 6 K, are depicted in Figure 7 along with the respective transmission integral fits, the respective fit data is listed in Table 5. The 300 and 78 K spectra can be reproduced with two components with isomer shifts of $\delta_{300K} = -7.27(6)$ and $+1.80(5)$ mm s^{-1} and $\delta_{78K} = -7.47(3)$ and $+1.84(2)$ mm s^{-1}. Quadrupole splitting parameters of $\Delta E_Q = 6.8(1)$ for Eu^{2+} and 3.4(2) mm s^{-1} for Eu^{3+} are observed at 78 K, consistent with the asymmetric coordination environment (Figure 3). The experimental line widths are $\Gamma = 2.69(7)$ and 2.3(1) mm s^{-1} for Eu^{2+}

and Eu^{3+}, respectively and in the typical range for Eu compounds.[52,64] The observed isomer shifts are clearly indicative of both, divalent and trivalent europium, the refined area ratios are 62 and 38% (Eu^{2+}/Eu^{3+}). This is perfectly in line with the magnetochemical investigations (*vide supra*) and the XANES data.[44] The observed isomer shift of the divalent species is in agreement with shifts observed for numerous Eu-intermetallics, e.g. $Eu_2Pt_6Al_{15}$ (78 K data, $\delta(Eu^{2+}) = -7.93(3)$ mm s^{-1}, $\delta(Eu^{3+}) = -1.70(3)$ mm s^{-1}),[52] showing a valence phase transition near 45 K, $EuIr_2Si_2$ ($\delta = -5.94$ mm s^{-1}),[65] $EuIr_{1.875}Pd_{0.125}Si_2$ (293 K: $\delta = -6.79$ mm s^{-1}),[65] or $EuIrMg_2$ (78 K: $\delta = -7.50(2)$ mm s^{-1}). The observed Eu^{3+} isomer shift is higher (more positive) compared

Table 5. Fitting parameters of the ^{151}Eu Mößbauer spectra of $Eu_2Ni_8Si_3$ (space group $P4_2/nmc$, $Z=4$) measured at 78 and 6 K. δ: isomer shift; Γ: experimental line width; ΔE_Q: quadrupole splitting; B_{hf}: magnetic hyperfine field; A: signal area ratio. The parameter marked with the asterisk was kept fixed during the fitting procedure.

T [K]	Ion	δ [mm s^{-1}]	Γ [mm s^{-1}]	ΔE_Q [mm s^{-1}]	B_{hf} [T]	A [%]
300 K	Eu^{2+}	−7.27(6)	6.2(3)	2.5(2)	–	60(1)
	Eu^{3+}	+1.80(5)	2.5(3)	2.3*	–	40(1)
78 K	Eu^{2+}	−7.47(3)	6.8(1)	2.69(7)	–	62(1)
	Eu^{3+}	+1.84(2)	3.4(2)	2.3(1)	–	38(1)
6 K	Eu^{2+}	−8.36(5)	−0.7(3)	4.0(1)	28.4(1)	68(1)
	Eu^{3+}	+2.02(3)	3.7(2)	2.7(1)	–	32(1)

EurJIC
European Journal of Inorganic Chemistry

Full Papers
doi.org/10.1002/ejic.202100564

Chemistry Europe
European Chemical
Societies Publishing

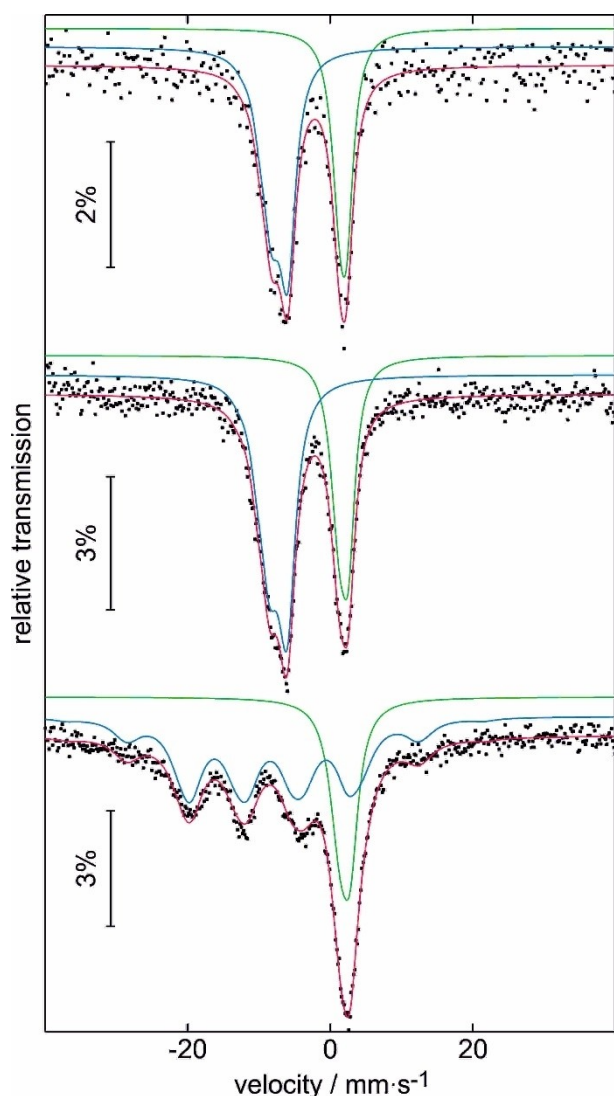**Figure 7.** Experimental (data points) and simulated (solid curves; blue Eu^{2+}, green Eu^{3+}) ^{151}Eu Mößbauer spectra of $Eu_2Ni_8Si_3$, measured at 300 (top), 78 (middle) and 6 K (bottom). The red line corresponds to the sum of the different signals used for fitting.

the Eu atoms in the two different valence states.[69] The enhanced line width of the Eu^{2+} signal ($\Gamma = 4.0(1)$ mm s^{-1}) is not inconsistent with the fact that only one Eu position is present. Furthermore, a correlation of the electric field gradient (78 K: $\Delta E_Q(Eu^{2+}) = 6.8(1)$ mm s^{-1}; 6 K: ($\Delta E_Q(Eu^{3+}) = -0.7(3)$ mm s^{-1}) and the line width is possible. Such a scenario usually arises near the magnetic ordering temperature and can be fitted using a distribution of magnetic hyperfine fields, as shown for the Eu-containing *Zintl*-phases $Eu_5In_2Pn_6$ ($Pn = As$, Sb)[70] and $Eu_{14}AlPn_{11}$ ($Pn = As$, Sb).[71]

2.5. ^{27}Al and ^{195}Pt Solid State NMR Spectroscopy

Figure 8 shows the field dependent ^{27}Al MAS-NMR spectra obtained for $Sr_2Pt_3Al_8$. Consistent with the crystal structure, the spectra confirm the presence of the three crystallographically unique sites Al1, Al2, and Al3 in the approximate ratio of 1:2:1. The $B_0 = 5.64$ T spectra are characterized by substantial line broadening effects arising from strong nuclear electric quadrupolar interactions, which can be described by second-order perturbation theory. At the higher field strength ($B_0 = 14.1$ T), the broadening is less pronounced, as expected. A consistent deconvolution of the data recorded at both field strengths is shown in Figure 8, and the corresponding interaction parameters, the quadrupolar coupling constants C_Q and the electric field gradient asymmetry parameter η_Q as well as the values δ_{iso}^{ms} due to magnetic (de)shielding effects are listed in Table 6. The magnetic shielding interaction is dominated by the unpaired s-electron spin density at the Fermi level as probed by the ^{27}Al nuclei (*Knight* shift). The quadrupolar interaction parameters are found to be in good agreement with theoretically calculated values, based on which the peak assignment is suggested. In particular, the results confirm that one of the Al
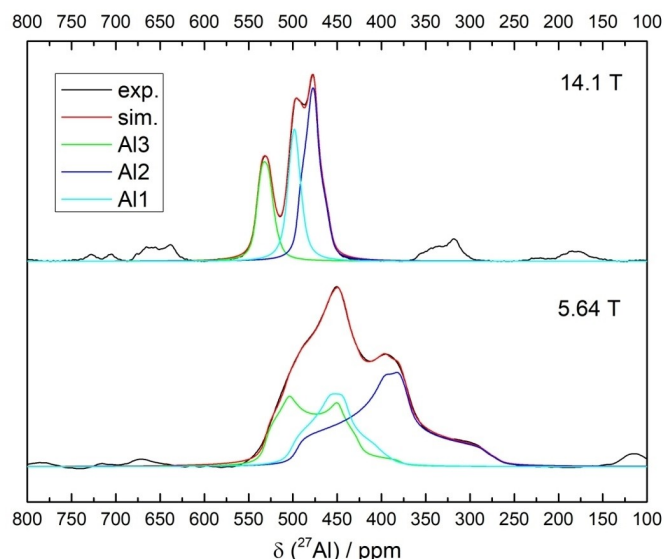
to trivalent ionic compounds such as EuF_3 ($\delta = -0.6(1)$ mm s^{-1}),[64a] Eu_2O_3 ($\delta = +0.2(1)$ mm s^{-1})[64a] or $Eu_2Ta_2O_{7.1}N_{0.6}$ ($\delta = +0.6(1)$ mm s^{-1})[64b] and also higher than the isomer shifts found in the rare trivalent intermetallic representatives $EuFe_2Si_2$ ($\delta = -0.7$ mm s^{-1}),[66] $EuCo_2Si_2$ ($\delta = -0.5$ mm s^{-1}),[66] $EuIr_{1.875}Pd_{0.125}Si_2$ (6 K: $\delta = -1.43$ mm s^{-1}),[65] $EuRu_2Si_2$ ($\delta = +0.4$ mm s^{-1}),[67] $EuRh_2Si_2$ ($\delta = +0.4$ mm s^{-1})[67-68] or $Eu_2Ir_3Al_9$ ($\delta = -0.34(8)$ mm s^{-1}).[64h] However, in the case of the intermetallic binaries $EuRh_2$ and $EuPd_3$, isomer shifts of $\delta = +3.0(2)$ mm s^{-1} and even $\delta = +4.6(2)$ mm s^{-1} (isomer shifts referenced to a $^{151}SmF_3$ source) have been observed, respectively.[64g] At 6 K, well below the Curie temperature, the Eu^{2+} signal shows a full hyperfine field splitting with $B_{hf} = 28.4(1)$ T, due to the magnetic ordering, while the Eu^{3+} signal remains unchanged. However, the Eu^{2+} to Eu^{3+} ratio changes again to 68:32%, underlining the presence of a difference in the Lamb-Mößbauer factors for

Figure 8. ^{27}Al MAS-NMR spectra of $Sr_2Pt_3Al_8$ at magnetic flux densities of $B_0 = 14.1$ and 5.64 T. Simulated spectra are based on the parameters listed in Table 5. Minor peaks are spinning sidebands.

EurJIC
European Journal of Inorganic Chemistry

Full Papers
doi.org/10.1002/ejic.202100564

Chemistry
Europe
European Chemical
Societies Publishing

Table 6. ^{27}Al isotropic shifts due to magnetic (de)shielding effects, δ_{ms}^{iso}, quadrupolar coupling constants, C_Q, and electric field gradient asymmetry parameters, η_Q, of $Sr_2Pt_3Al_8$ ($P4_2/nmc$) determined from line shape fits at $B_0 = 14.1T/5.64T$. Theoretically calculated values are given in parentheses.

	δ_{ms}^{iso}/ppm ±1	C_q/MHz ±0.1	η ±0.05	[%] (±2)
Al1	505	5.3/5.3(+5.589)	0.85/0.71(0.969)	29/24
Al2	495	7.6/7.4(−6.344)	0.76/0.85(0.970)	47/47
Al3	543	6.6/6.7(+6.027)	0.29/0.44(0.296)	25/29

sites (Al3) is characterized by a much smaller value of the electric field asymmetry parameter than the other sites. Overall, the very good agreement between theoretically calculated and experimentally determined electric field gradient tensors serves as an important validation of the compound's crystal structure.

Figure 9 shows the ^{195}Pt NMR spectra, which confirm the quantitative 1:2 ratio of the platinum sites. The two sites are characterized by a very large difference in the magnitude of the *Knight* shift, which is much more negative for Pt2 than for Pt1. At spinning speeds of 15.0, 25.0, and 35.0 kHz, we measured $\delta_{iso}^{ms} = -554, -526$ and -504 ppm for Pt1, and $-2733, -2730$, and -2721 ppm for Pt2. We attribute these variations to temperature changes as a function of spinning speed. Furthermore, the ^{195}Pt resonance of Pt2 is characterized by a large magnetic shielding anisotropy $\Delta\sigma = \delta_{zz} - 1/2(\delta_{xx} + \delta_{yy}) = -1500 \pm 100$ ppm, using the convention $|\delta_{zz} - \delta_{iso}| > |\delta_{xx} - \delta_{iso}| > |\delta_{yy} - \delta_{iso}|$, reflecting the lower point symmetry of this site compared to the more symmetric environment of Pt1 ($\Delta\sigma = -800 \pm 100$ ppm). Both sites also differ significantly in the value of the magnetic shielding asymmetry parameter $\eta = (\delta_{xx} - \delta_{yy})/(\delta_{zz} - \delta_{iso}) = 0.45(5)$ and 0.8(1) for Pt1 and Pt2, respectively.

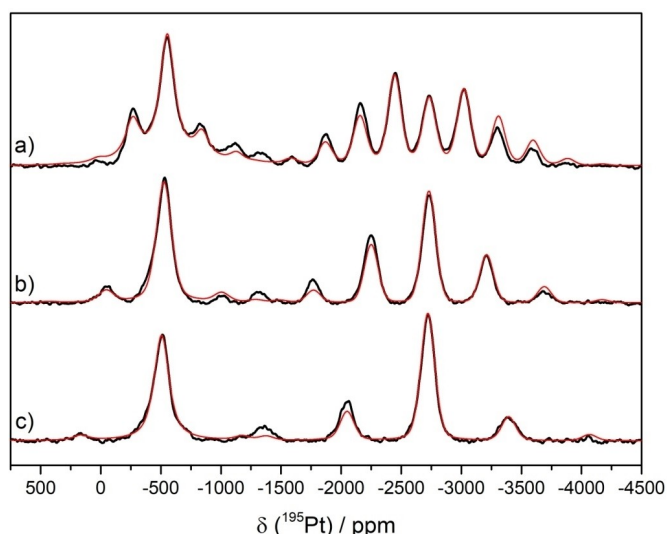**Figure 9.** ^{195}Pt MAS-NMR spectra (black trace) of $Sr_2Pt_3Al_8$ at $B_0 = 5.64$ T and three different spinning speeds a) 15.0 kHz, b) 25.0 kHz, c) 35.0 kHz. Simulations of the spinning sideband manifold are shown as red traces, based on the magnetic shielding tensor components described in the text.

2.6. Theoretical Calculations

The chemical bonding in $Sr_2Pt_3Al_8$ was investigated via crystal orbital Hamiltonian population (COHP) analysis. The values of the integrated COHP (ICOHP) in Table 7 show that the Pt—Al bonds (more than 50% contributions to the total ICOHP value) in $Sr_2Pt_3Al_8$ are the dominant interactions, followed by Al—Al and the weak Sr—Al and Sr—Pt interactions. Especially the differences in the strength of the Pt—Al (−1.56 to −2.50 eV) and Al—Al interactions (−0.68 to −1.67 eV) compared to the Sr—Al (−0.20 to −0.51 eV) and Sr—Pt (−0.26 to −0.46 eV) ones suggest a polyanionic $[Pt_3Al_8]^{\delta-}$ network, while $Sr^{\delta+}$ cations reside in the resulting cavities. The polyanionic $[Pt_3Al_8]^{\delta-}$ network contains [Pt—Al] tubes along the c axis, which are linked with Al3—Al3 and Pt2—Al bonds to form a 3D substructure (Figure 10). The strength of −2.50 eV is observed for the Pt2—Al2 bond and significantly exceeds the strength of all Pt—Al interactions observed in $Ba_3Pt_4Al_4$ (−1.47 to −2.01 eV)[24] and $SrPtAl_2$ (−1.94 and −2.02 eV).[28] Even higher bond strengths of −3.09 eV (Pt4—Al9) have been observed in $Ba_6Pt_{22}Al_{53}$.[72]

The calculated Bader effective charges for $Sr_2Pt_3Al_8$ are listed in Table 8. Sr and Al atoms have positive charges, while the Pt atoms have negative charges. The charges found on the Sr atoms are less than +2 (+1.21), indicating the presence of some weak covalent bonding interactions between Sr and the Pt—Al network, in agreement with the small negative ICOHP values of the Sr—Pt and Sr—Al interactions. Also, the fact that all Al atoms have charges far from +3 (+1.62, +1.17, and +0.67) indicates that the Pt—Al interactions have more covalent character than ionic, in accordance with the large negative ICOHP values thus supporting the polyanionic $[Pt_3Al_8]^{\delta-}$ network. Finally, the Pt atoms exhibit Bader charges of −3.86 and −3.91. These values significantly exceed the ones in $Ba_3Pt_4Al_4$ (−2.39 to −2.42),[24] however, they are similar to the ones calculated for the MPtAl$_2$ series (M = Ca—Ba; −3.53 to −3.42).[28] This can be explained by the differences in the composition of the polyanion and therefore a significantly different electron transfer.

3. Conclusions

Tetragonal $Sr_2Pt_3Al_8$ and structurally related $Eu_2Ni_8Si_3$ (both space group $P4_2/nmc$) were synthesized from the elements and characterized via powder and single crystal X-ray diffraction experiments. For the aluminum compound full atomic ordering was observed, for the silicide Si/Ni mixing was seen during the structure refinement. Magnetic measurements revealed a tem-

EurJIC
European Journal of Inorganic Chemistry

Full Papers
doi.org/10.1002/ejic.202100564

Chemistry
Europe
European Chemical
Societies Publishing

Table 7. Atomic interactions, distances up to 400 pm and their corresponding integrated COHPs (ICOHPs) in eV/bond and eV/f.u. of Sr$_2$Pt$_3$Al$_8$ (anti-Eu$_2$Ni$_8$Si$_3$ type, space group $P4_2/nmc$, $Z=4$).

Interaction	Counts	Distance	ICOHP/bond	ICOHP/f.u.
Sr−Pt1	2	334.7	−0.46	−0.92
Sr−Pt2	4	352.0	−0.42	−1.68
	4	373.3	−0.26	−1.04
Sr−Al1	2	343.3	−0.34	−0.68
	4	372.0	−0.20	−0.80
Sr−Al2	4	314.0	−0.35	−1.40
	4	332.8	−0.42	−1.68
	4	334.5	−0.50	−2.00
Sr−Al3	4	328.3	−0.51	−2.04
Sr−Sr	2	384.6	−0.13	−0.26
SUM				**−12.5 (14.8%)**
Pt1−Al1	2	252.6	−2.38	−4.76
	2	258.2	−2.32	−4.64
Pt1−Al2	4	266.6	−1.76	−7.04
Pt2−Al1	4	278.7	−1.56	−6.24
Pt2−Al2	4	251.7	−2.50	−10.0
	4	266.0	−1.77	−7.08
Pt2−Al3	4	258.7	−1.91	−7.64
SUM				**−47.4 (56.3%)**
Al1−Al1	1	302.6	−0.68	−0.68
Al1−Al2	4	284.1	−0.86	−3.44
	4	286.1	−1.01	−4.04
Al1−Al3	2	274.9	−1.08	−2.16
Al2−Al2	2	279.9	−1.18	−2.36
	2	283.1	−0.94	−1.88
Al2−Al3	4	268.1	−1.44	−5.76
Al3−Al3	1	267.3	−1.67	−1.67
	2	271.2	−1.15	−2.30
SUM				**−24.3 (28.9%)**
Overall ICOHP				**−84.2**

perature independent behavior for the Sr compound, while a ferromagnetic transition at $T_C = 46.9(2)$ K was detected for the Eu compound. For the latter, a significantly reduced effective magnetic moment of $\mu_{eff} = 6.61(1)$ μ$_B$ per Eu atom was obtained

from Curie-Weiss fits, suggesting an intermediate valence state. Subsequently, this was proven by ^{151}Eu Mößbauer spectroscopic investigations showing Eu^{2+}/Eu^{3+} ratios of 60%/40% (300 K) along with slight variations (78 K: 62%/38%; 6 K: 68%/32%)
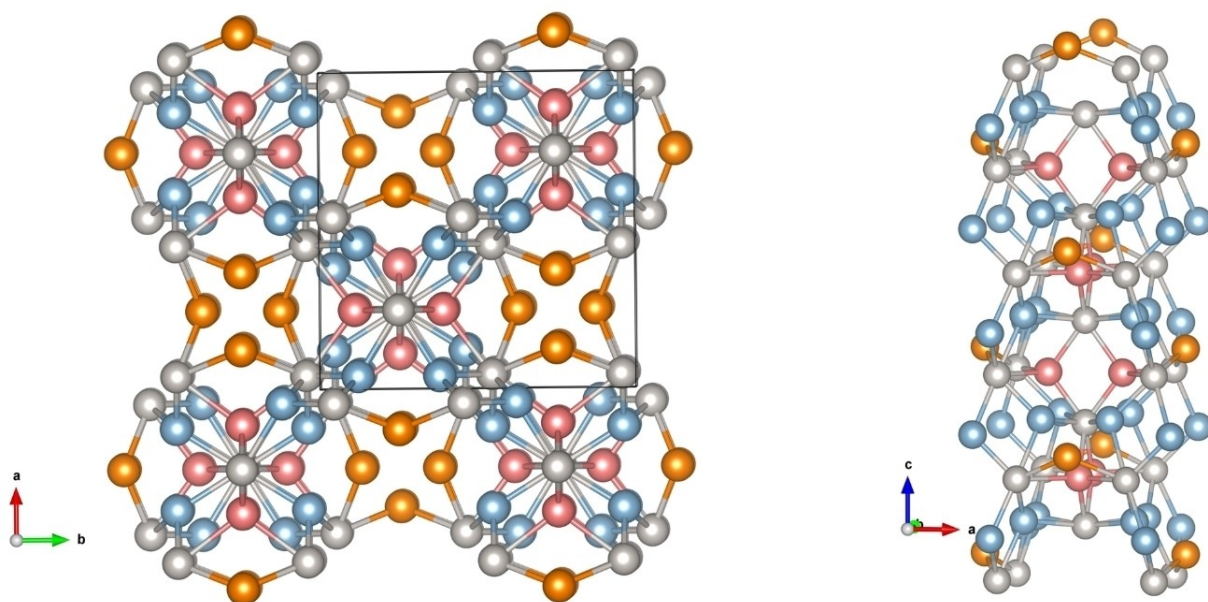

Figure 10. Pt−Al network in Sr$_2$Pt$_3$Al$_8$. Perspective view along the crystallographic c axis (left), and one tube of the network in the c direction (right). Pink, blue, orange, and gray spheres represent Al1, Al2, Al3 and Pt atoms.

EurJIC
European Journal of Inorganic Chemistry

Full Papers
doi.org/10.1002/ejic.202100564

Chemistry Europe
European Chemical
Societies Publishing

Table 8. Bader Charges in $Sr_2Pt_3Al_8$ (*anti*-$Eu_2Ni_8Si_3$ type, space group $P4_2/nmc$, $Z = 4$).

Atom	Charge	Atom	Charge
Sr	+1.21	Al1	+1.62
Pt1	−3.86	Al2	+1.17
Pt2	−3.91	Al3	+0.67

Table 9. Reaction products, based on powder X-ray diffraction patterns, of the synthetic attempts to yield the '$M_2Pt_3Al_8$' phases with M=Ca, Ba, Eu and Yb.

Target composition	Main products
$Ca_2Pt_3Al_8$	$Ca_2Pt_3Al_9$[74]
$Ba_2Pt_3Al_8$	unknown
$Eu_2Pt_3Al_8$	$Eu_2Pt_3Al_9$[74] and $Eu_2Pt_6Al_{15}$[52]
$Yb_2Pt_3Al_8$	$Yb_2Pt_3Al_9$[74] and $Yb_4Pt_9Al_{24}$[75]

that could be attributed to differences in the Lamb Mößbauer factors. The determined ratios are perfectly in line with the observed reduced magnetic moment. Below the *Curie* temperature, the Eu^{2+} signal furthermore shows a full magnetic hyperfine splitting, with an internal magnetic field value of $B_0 = 28.4$ T. Due to the diamagnetic nature of $Sr_2Pt_3Al_8$, the crystallographically independent Al and Pt sites could be characterized by ^{27}Al and ^{195}Pt solid-state NMR spectroscopy. The site multiplicities of the Al sites with a 1:2:1 ratio could be observed in the ^{27}Al spectra along with the 1:2 ratio of the two crystallographically distinct Pt sites in the ^{195}Pt spectra. The asymmetries in the coordination environments of the Al atoms are also reflected in the values of the quadrupolar coupling constants and electric field gradient asymmetry parameters. Theoretical calculations confirm the experimentally determined NMR parameters. COHP bonding and Bader charge analyses finally show that the $Sr_2Pt_3Al_8$ compound is built of polyanionic $[Pt_3Al_8]^{\delta-}$ network interacting with $Sr^{\delta+}$ cations.

Experimental Section

Synthesis

Few well-shaped single crystals of $Sr_2Pt_3Al_8$ (Figure 11, left) were first obtained during attempts to grow single crystals of $SrPtAl_2$.[28] X-ray phase-pure samples of $Sr_2Pt_3Al_8$ and $Eu_2Ni_8Si_3$ were subsequently prepared from the elements: dendritic strontium pieces (onyxmet, 99%), europium pieces (American Elements, 99.99%), nickel wire (Alfa Aesar, 99.5%), platinum sheets (Agosi, 99.9%) and aluminum turnings (Koch Chemicals, 99.99%). For $Sr_2Pt_3Al_8$, the elements were sealed into tantalum ampules via arc-welding[73] in an argon atmosphere of about 800 mbar. The argon gas was purified over titanium sponge (873 K), molecular sieves and silica gel. The strontium pieces were cleaned mechanically under dry cyclohexane and stored under argon prior to use. The tantalum ampules were subsequently enclosed into evacuated fused silica tubes and placed in a box furnace (Nabertherm). The samples were heated to 1373 K, held at this temperature for 2 h followed by slow cooling (5 Kh⁻¹) to 873 K. They were kept at this temperature for one week and again slowly cooled (5 Kh⁻¹) to room temperature. $Sr_2Pt_3Al_8$ shows a metallic luster and is grey in its powdered form. No sensitivity to moisture or air was observed over several days and weeks. Attempts to synthesize supposedly isotypic Ca, Ba, Eu and Yb compounds were not successful under the chosen synthetic conditions (Table 9). $Eu_2Ni_8Si_3$ (Figure 11, right) was prepared directly from the elements by arc-melting[73] a 2.05:8:3 (Eu:Ni:Si) elemental ratio in a water-cooled copper-hearth in an argon atmosphere of about 800 mbar. Due to the low boiling point of Eu, a slight excess was used. The as-obtained button was subsequently enclosed in a quartz tube and annealed at 1073 K for two weeks in a tube furnace followed by water quenching.

EDX analysis

A semiquantitive EDX analysis was conducted on a Zeiss Evo MA10 scanning electron microscope with an Oxford Instrument EDX detector using SrF_2, Pt, Al_2O_3, EuF_3, SiO_2 and Ni as internal standards. The experimentally observed composition of the investigated $Sr_2Pt_3Al_8$ single crystal (Sr: 14(2) at.%; Pt: 24(2) at.%; Al: 62(2) at.%) was close to the theoretical one (15.4 at.% Sr;
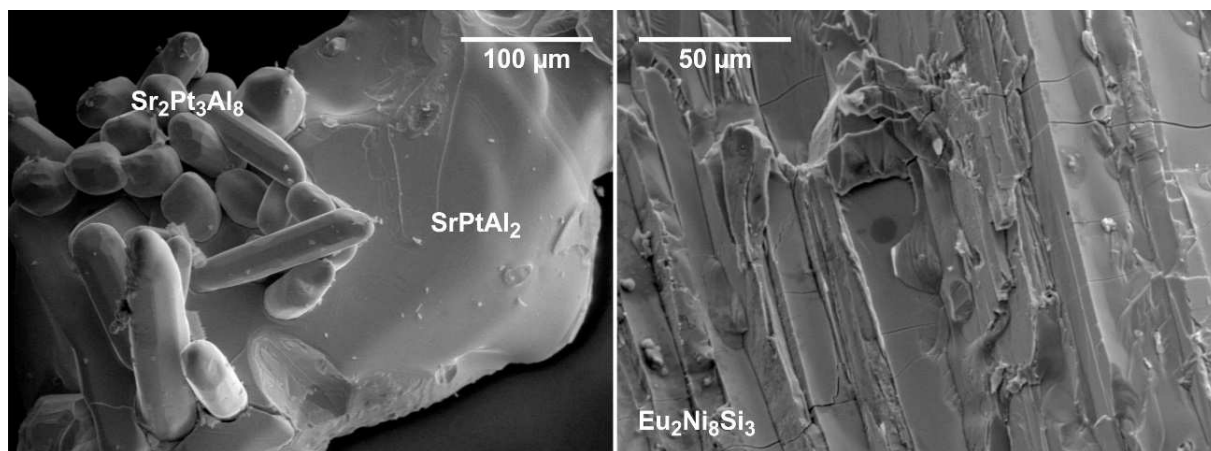

Figure 11. Scanning electron microscopic (SEM) images of (left) pieces obtained from a synthesis with nominal composition '$SrPtAl_2$'. Besides the platelet-shaped crystals of $SrPtAl_2$, also needle-shaped crystals of $Sr_2Pt_3Al_8$ are visible and (right) an annealed ingot of $Eu_2Ni_8Si_3$, also indicating needle-shaped crystallites.

EurJIC
European Journal of Inorganic Chemistry

Full Papers
doi.org/10.1002/ejic.202100564

Chemistry Europe
European Chemical
Societies Publishing

23.1 at.% Pt; 61.5 at.% Al); for $Eu_2Ni_8Si_3$ (experimental: 15(2) at.% Eu; 60(2) at.% Ni; 25(2) at.% Si; theoretical: 15.4 at.% Eu; 61.5 at.% Ni; 23.1 at.% Si) similar deviations were observed. No impurity elements heavier than sodium (detection limit) were detected. Due to conchoidal fracture the standard uncertainties for single crystals are 2 at.%.

Powder X-Ray diffraction

$Sr_2Pt_3Al_8$ and $Eu_2Ni_8Si_3$ were characterized by Guinier powder patterns (imaging plate technique, Fuji film, BAS-READER 1800) using $CuK\alpha1$ radiation and α-quartz ($a = 491.0$, $c = 540.46$ pm) as an internal standard. Least-squares refinements of the obtained diffractograms led to tetragonal lattice parameters of $a = 1082.9(2)$ pm, $c = 823.3(2)$ pm for $Sr_2Pt_3Al_8$ and $a = 997.9(1)$ and $c = 747.6(1)$ pm for $Eu_2Ni_8Si_3$, respectively. Correct indexing of the experimental diffraction patterns was ensured by comparison with the calculated ones[76] obtained from single crystal diffraction experiments (see below) and literature data of $Eu_2Ni_8Si_3$.[44]

Single crystal X-Ray diffraction

Well-shaped single crystals of $Sr_2Pt_3Al_8$ were obtained as a side-product of a reaction targeting $SrPtAl_2$. Single crystals of $Eu_2Ni_8Si_3$ were obtained from direct attempts to obtain this compound. They were fixed to thin quartz fibers using beeswax and investigated by Laue photographs on a Buerger precession camera (white Mo-radiation, imaging plate technique, Fujifilm, BAS-1800). Intensity data sets of suitable single crystals were collected on a Stoe IPDS-II diffractometer (graphite monochromatized $MoK\alpha$ radiation; oscillation mode). A numerical absorption correction was applied to the data sets. Information about data collection, structure refinements, atomic coordinates and interatomic distances are listed in Tables 2–4.

Mößbauer spectroscopy

The 21.53 keV transition of ^{151}Eu with an activity of 65 MBq (1% of the total activity of a $^{151}Sm:EuF_3$ source) was used for the ^{151}Eu Mößbauer spectroscopic experiments, which were conducted in the usual transmission geometry. The measurements were performed with a continuous flow cryostat system (Janis Research Co LLC). The temperature of the absorber was set to 6 K and 78 K, while the source was kept at room temperature. The temperature was controlled by a resistance thermometer (~0.5 K accuracy). The sample was enclosed in a small PMMA container, the required sample mass was calculated based on the work by Long et al.[77] Fitting of the spectrum was performed with the WinNormos for Igor6 program package.[78] The obtained fitting parameters are listed in Table 5.

^{27}Al and ^{195}Pt Solid-State NMR Spectroscopy

Field dependent ^{27}Al solid-state MAS NMR spectra were recorded with Bruker Avance Neo ($B_0 = 14.1$ T) and Agilent DD2 ($B_0 = 5.64$ T) NMR spectrometers. To reduce the electrical conductivity and density the finely powdered samples were mixed in approximate volume ratios of 1:2 with dry potassium bromide and filled into conventional ZrO_2-MAS rotors with 1.3 or 1.6 mm diameters, depending on the two different spectrometers. The spectra were recorded using conventional single-pulse experiments with typical pulse-lengths of 0.36 μs (corresponding to flip-angles below 30°), relaxation delays of 0.5 s and MAS spinning frequencies between 20 and 35 kHz. Solid AlF_3 was used as a secondary standard (−16 ppm), referring to a 1 molar aqueous solution of $Al(NO_3)_3$.

^{195}Pt solid-state MAS NMR spectra of $Sr_2Pt_3Al_9$ were obtained at 52.1 MHz on an Agilent DD2 spectrometer operating at $B_0 = 5.64$ T and equipped with a 1.6 mm rotor. The spectra were measured with a rotor-synchronized Hahn echo after one rotor cycle at spinning speeds between 15.0 and 35.0 kHz with 90 and 180° excitation pulses of 2.5 and 5.0 μs length, respectively, and relaxation delays between 0.1 and 0.5 s. All spectra are referenced relative to solid K_2PtCl_6, the data is summarized in Table 6.

Theoretical methodology

Electronic structure calculations of $Sr_2Pt_3Al_8$ were performed using the projector augmented wave method (PAW) of Blöchl[79] coded in the Vienna *ab initio* simulation package (VASP).[80] All VASP calculations employed the generalized gradient approximation (GGA) with exchange and correlation treated by Perdew-Burke-Enzerhof (PBE).[81] The cutoff energy for the plane wave calculations was set to 500 eV and the Brillouin zone integration was carried out using $3 \times 5 \times 7$ Γ-centered k-point meshes. The Bader charge analysis was based on VASP calculations with subsequent calculations with the Bader program developed by the Henkelman group.[82] Chemical bonding was assessed via crystal orbital Hamiltonian population (COHP) analysis using the Stuttgart version of the tight-binding, linear muffin-tin orbital (TB-LMTO) method with the atomic spheres approximation.[83] Within TB-LMTO, exchange and correlation were treated using the von Barth-Hedin local density approximation (LDA). All relativistic effects except spin-orbit coupling were taken into account using a scalar relativistic approximation.[84] The basis sets were 5s/(5p)/4d/(4f) for Sr, 6s/6p/5d/(5f) for Pt, and 3s/3p/(3d) for Al, with orbitals in parentheses down-folded.[85] The Brillouin zone was sampled by 75 k-points. The data obtained from quantum chemical calculations is summarized in Table 7 and Table 8.

Deposition Numbers 1863339 (for $Sr_2Pt_3Al_8$) and 2089980 (for $Eu_2Ni_{7.82(2)}Si_{3.18(2)}$) contain the supplementary crystallographic data for this paper. These data are provided free of charge by the joint Cambridge Crystallographic Data Centre and Fachinformationszentrum Karlsruhe Access Structures service www.ccdc.cam.ac.uk/structures.

Conflict of Interest

The authors declare no conflict of interest.

Keywords: Intermetallics · Magnetism · Mößbauer spectroscopy · NMR spectroscopy · X-ray diffraction

[1] P. Villars, K. Cenzual in *Pearson's Crystal Data: Crystal Structure Database for Inorganic Compounds (on DVD)*, Vol. ASM International®, Materials Park, Ohio (USA), **release 2019/2020**.

[2] a) G. Cordier, T. Friedrich, *Z. Kristallogr.* **1993**, *205*, 135–136; b) G. Cordier, T. Friedrich, R. Henseleit, A. Grauel, U. Tegel, C. Schank, C. Geibel, *J. Alloys Compd.* **1993**, *201*, 197–201.

[3] I. Doverbratt, S. Ponou, Y. Zhang, S. Lidin, G. J. Miller, *Chem. Mater.* **2015**, *27*, 304–315.

[4] S. Schoolaert, W. Jung, *Z. Anorg. Allg. Chem.* **2002**, *628*, 1806–1810.

[5] G. Cordier, G. Dörsam, T. Friedrich, R. Henseleit, C. Röhr, *J. Alloys Compd.* **1993**, *190*, 201–207.

[6] a) P. Kenfack Tsobnang, D. Fotio, S. Ponou, C. Fon Abi, *Acta Crystallogr.* **2011**, *E67*, i55; b) F. Hulliger, *J. Alloys Compd.* **1993**, *196*, 225–228.

[7] C. B. Shoemaker, D. P. Shoemaker, *Acta Crystallogr.* **1965**, *18*, 900–905.

[8] a) G. Cordier, T. Friedrich, *Z. Kristallogr.* **1992**, *201*, 306–307; b) G. Cordier, G. Dörsam, C. Röhr, *J. Less-Common Met.* **1990**, *166*, 115–124.

[9] Z. Ban, M. Sikirica, *Acta Crystallogr.* **1965**, *18*, 594–599.

[10] J. Pham, A. Kreyssig, A. I. Goldman, G. J. Miller, *Inorg. Chem.* **2016**, *55*, 10425–10437.

[11] S. E. Latturner, D. Bilc, S. D. Mahanti, M. G. Kanatzidis, *Inorg. Chem.* **2009**, *48*, 1346–1355.

[12] B. Chabot, N. Engel, E. Parthé, *Acta Crystallogr.* **1981**, *B37*, 671–673.

[13] F. Hulliger, *J. Alloys Compd.* **1995**, *218*, 255–258.

[14] A. Palasyuk, Y. Grin, G. J. Miller, *J. Am. Chem. Soc.* **2014**, *136*, 3108–3117.

[15] G. Cordier, C. Röhr, *J. Less-Common Met.* **1991**, *170*, 333–357.

[16] I. Zeiringer, N. Melnychenko-Koblyuk, A. Grytsiv, E. Bauer, G. Giester, P. Rogl, *J. Phase Equilib.* **2011**, *32*, 115–127.

[17] a) T. Mishra, Q. Lin, J. D. Corbett, *Inorg. Chem.* **2013**, *52*, 13623–13630; b) B. Gerke, R. Pöttgen, *Z. Naturforsch.* **2014**, *69b*, 121–124.

[18] B. Gerke, R.-D. Hoffmann, R. Pöttgen, *Z. Anorg. Allg. Chem.* **2013**, *639*, 2444–2449.

[19] a) F. Hulliger, H. U. Nissen, R. Wessicken, *J. Alloys Compd.* **1994**, *206*, 263–266; b) F. Stegemann, C. Benndorf, Y. Zhang, M. Bartsch, H. Zacharias, B. P. T. Fokwa, H. Eckert, O. Janka, *Z. Anorg. Allg. Chem.* **2017**, *643*, 1379–1390.

[20] B. Eisenmann, N. May, W. Müller, H. Schäfer, *Z. Naturforsch.* **1972**, *27b*, 1155–1157.

[21] B. Gerke, R. Pöttgen, *Z. Naturforsch.* **2015**, *70b*, 903–909.

[22] V. Smetana, G. J. Miller, J. D. Corbett, *Inorg. Chem.* **2012**, *51*, 7711–7721.

[23] N. C. Baenziger, J. W. Conant, *Acta Crystallogr.* **1956**, *9*, 361–364.

[24] F. Stegemann, C. Benndorf, T. Bartsch, R. S. Touzani, M. Bartsch, H. Zacharias, B. P. T. Fokwa, H. Eckert, O. Janka, *Inorg. Chem.* **2015**, *54*, 10785–10793.

[25] V. Smetana, S. Steinberg, Y. Mudryk, V. Pecharsky, G. J. Miller, A.-V. Mudring, *Inorg. Chem.* **2015**, *54*, 10296–10308.

[26] E. Zintl, W. Haucke, *Z. Elektrochem. Angew. Phys. Chem.* **1938**, *44*, 104–111.

[27] M. Radzieowski, F. Stegemann, R.-D. Hoffmann, O. Janka, *Z. Kristallogr.* **2017**, *232*, 675–687.

[28] F. Stegemann, T. Block, S. Klenner, Y. Zhang, B. P. T. Fokwa, A. Timmer, H. Mönig, C. Doerenkamp, H. Eckert, O. Janka, *Chem. Eur. J.* **2019**, *25*, 10735–10747.

[29] a) B. Heying, R.-D. Hoffmann, R. Pöttgen, *Z. Naturforsch.* **2005**, *60b*, 491–494; b) H. Perlitz, A. Westgren, *Ark. Kemi Mineral. Geol.* **1943**, *16B*, 1–5.

[30] R. Glaum, J. H. Albering, W. Jeitschko, L. Boonk, *J. Alloys Compd.* **1992**, *185*, 301–309.

[31] F. Stegemann, C. Benndorf, R. S. Touzani, B. P. T. Fokwa, O. Janka, *J. Solid State Chem.* **2016**, *242*, 143–150.

[32] F. Stegemann, C. Benndorf, R. S. Touzani, B. P. T. Fokwa, O. Janka, *Eur. J. Inorg. Chem.* **2016**, *2016*, 1108–1114.

[33] R.-D. Hoffmann, F. Stegemann, O. Janka, *Z. Kristallogr.* **2016**, *231*, 127–142.

[34] Y. B. Kuz'ma, P. I. Krypyakevych, N. S. Bilonizhko, *Dopov. Akad. Nauk Ukr. RSR* **1969**, *A31*, 939–941.

[35] C. Benndorf, F. Stegemann, S. Seidel, L. Schubert, M. Bartsch, H. Zacharias, B. Mausolf, F. Haarmann, H. Eckert, R. Pöttgen, O. Janka, *Chem. Eur. J.* **2017**, *23*, 4187–4196.

[36] K. Klepp, E. Parthé, *Acta Crystallogr.* **1982**, *B38*, 1541–1544.

[37] J. Emsley, *The Elements*, Clarendon Press, Oxford University Press, Oxford, New York, **1998**.

[38] K. Turban, H. Schäfer, *J. Less-Common Met.* **1975**, *40*, 91–96.

[39] M. B. Manyako, O. S. Zarechnyuk, T. I. Yanson, *Kristallografiya* **1987**, *32*, 1389–1391.

[40] Y. P. Yarmolyuk, R. M. Pykhal, O. S. Zarechnyuk, *Tezizy Dokl. Vses. Konf. Kristallokhim. Intermet. Soeden* **1974**, *2*, 39–40.

[41] M. B. Manyako, T. I. Yanson, O. S. Zarechnyuk, *Russ. Metall.* **1988**, *3*, 195–188.

[42] R. E. Marsh, K. M. Slagle, *Acta Crystallogr.* **1988**, *C44*, 395–396.

[43] Q. A. Zhang, W. M. Yang, Q. Y. Hou, H. Y. Wu, *Intermetallics* **2005**, *13*, 796–799.

[44] B. D. Belan, V. K. Belskii, V. K. Pecharsky, O. I. Bodak, T. V. Zukh, *Dopov. Akad. Nauk Ukr. RSR* **1986**, *12*, 63–65.

[45] L. Palatinus, G. Chapuis, *J. Appl. Crystallogr.* **2007**, *40*, 786–790.

[46] a) V. Petříček, M. Dušek, L. Palatinus in *Jana2006. The crystallographic computing system*, Vol. Institute of Physics, Praha, Czech Republic, **2006**; b) V. Petříček, M. Dušek, L. Palatinus, *Z. Kristallogr.* **2014**, *229*, 345–352.

[47] A. I. Tursina, N. G. Bukhan'ko, A. V. Gribanov, V. A. Shchelkunov, Y. V. Nelyubina, *Acta Crystallogr.* **2005**, *E61*, i285–i286.

[48] L. G. Akselrud, V. I. Yarovets, O. I. Bodak, Y. P. Yarmolyuk, E. I. Gladyshevskii, *Kristallografiya* **1976**, *21*, 383–386.

[49] R. E. Gladyshevskii, O. R. Strusievicz, K. Cenzual, E. Parthé, *Acta Crystallogr.* **1993**, *B49*, 474–478.

[50] F. Yuan, Y. Mozharivskyj, A. V. Morozkin, A. V. Knotko, V. O. Yapaskurt, M. Pani, A. Provino, P. Manfrinetti, *J. Solid State Chem.* **2014**, *219*, 247–258.

[51] A. W. Hull, *Phys. Rev.* **1917**, *10*, 661–696.

[52] M. Radziewski, F. Stegemann, T. Block, J. Stahl, D. Johrendt, O. Janka, *J. Am. Chem. Soc.* **2018**, *140*, 8950–8957.

[53] A. I. Tursina, E. V. Murashova, H. Noël, N. G. Bukhan'ko, Y. D. Seropegin, *Intermetallics* **2009**, *17*, 780–783.

[54] L.-E. Edshammar, *Acta Chem. Scand.* **1966**, *20*, 2683–2688.

[55] P. Debye, *Phys. Z.* **1917**, *18*, 483.

[56] H. Nowotny, H. Wesenberg, *Z. Metallkd.* **1939**, *31*, 363–364.

[57] E. J. Duwell, N. C. Baenziger, *Acta Crystallogr.* **1955**, *8*, 705–710.

[58] a) G. Nagorsen, H. Posch, H. Schäfer, A. Weiss, *Z. Naturforsch.* **1969**, *24b*, 1191; b) G. Cordier, E. Czech, H. Schäfer, *Z. Naturforsch.* **1982**, *24b*, 1191–1191.

[59] T. Heumann, M. Kniepmeyer, *Z. Anorg. Allg. Chem.* **1957**, *290*, 191–204.

[60] F. Simon, E. Vohsen, *Z. Phys. Chem.* **1928**, *133*, 165–187.

[61] E. E. Havinga, H. Damsma, P. Hokkeling, *J. Less-Common Met.* **1972**, *27*, 169–186.

[62] H. Lueken, *Magnetochemie*, B. G. Teubner, Stuttgart, Leipzig, **1999**, p.

[63] B. T. Matthias, R. M. Bozorth, J. H. Van Vleck, *Phys. Rev. Lett.* **1961**, *7*, 160–161.

[64] a) G. Gerth, P. Kienle, K. Luchner, *Phys. Lett. A* **1968**, *27*, 557–558; b) B. Anke, S. Hund, C. Lorent, O. Janka, T. Block, R. Pöttgen, M. Lerch, *Z. Anorg. Allg. Chem.* **2017**, *643*, 1824–1830; c) G. K. Shenoy, F. E. Wagner, *Mößbauer Isomer Shifts*, North-Holland Publishing Company, Amsterdam, **1978**; d) T. Harmening, R. Pöttgen, *Z. Naturforsch.* **2009**, *65b*, 90–94; e) E. Morsen, B. D. Mosel, W. Müller-Warmuth, M. Reehuis, W. Jeitschko, *J. Phys. C* **1988**, *21*, 3133; f) J.-P. Schmiegel, T. Block, B. Gerke, T. Fickenscher, R. S. Touzani, B. P. T. Fokwa, O. Janka, *Inorg. Chem.* **2016**, *55*, 9057–9064; g) H. H. Wickman, J. H. Wernick, R. C. Sherwood, C. F. Wagner, *J. Phys. Chem. Solids* **1968**, *29*, 181–182; h) F. Stegemann, T. Block, S. Klenner, O. Janka, *Chem. Eur. J.* **2019**, *25*, 3505–3509.

[65] L. Fournes, B. Chevalier, B. Lloret, J. Etourneau, *Z. Phys. B* **1989**, *75*, 501–505.

[66] I. Mayer, I. Felner, *J. Phys. Chem. Solids* **1977**, *38*, 1031–1034.

[67] I. Felner, I. Nowik, *J. Phys. Chem. Solids* **1984**, *45*, 419–426.

[68] B. Chevalier, J. M. D. Coey, B. Lloret, J. Etourneau, *J. Phys. C* **1986**, *19*, 4521–4528.

[69] P. Gütlich, E. Bill, A. X. Trautwein, *Mössbauer Spectroscopy and Transition Metal Chemistry*, Springer, Berlin, Heidelberg, **2011**.

[70] M. Radzieowski, F. Stegemann, S. Klenner, Y. Zhang, B. P. T. Fokwa, O. Janka, *Mater. Chem. Front.* **2020**, *4*, 1231–1248.

[71] M. Radzieowski, T. Block, S. Klenner, Y. Zhang, B. P. T. Fokwa, O. Janka, *Inorg. Chem. Front.* **2019**, *6*, 137–147.

[72] F. Stegemann, R. S. Touzani, O. Janka, *Dalton Trans.* **2019**, *48*, 14103–14114.

[73] R. Pöttgen, T. Gulden, A. Simon, *GIT Labor-Fachz.* **1999**, *43*, 133–136.

[74] F. Stegemann, Y. Zhang, B. P. T. Fokwa, O. Janka, *Dalton Trans.* **2020**, *49*, 6398–6406.

[75] V. M. T. Thiede, B. Fehrmann, W. Jeitschko, *Z. Anorg. Allg. Chem.* **1999**, *625*, 1417–1425.

[76] K. Yvon, W. Jeitschko, E. Parthé, *J. Appl. Crystallogr.* **1977**, *10*, 73–74.

[77] G. J. Long, T. E. Cranshaw, G. Longworth, *Mössbauer Eff. Ref. Data J.* **1983**, *6*, 42–49.

[78] R. A. Brand in *WinNormos for Igor6, Version for Igor 6.2 or above: 22.02.2017*, Vol. Universität Duisburg, Duisburg (Germany), **2017**.

[79] a) P. E. Blöchl, *Phys. Rev. B* **1994**, *50*, 17953–17979; b) G. Kresse, D. Joubert, *Phys. Rev. B* **1999**, *59*, 1758–1775.

[80] a) G. Kresse, J. Furthmüller, *Phys. Rev. B* **1996**, *54*, 11169–11186; b) G. Kresse, J. Furthmüller, *Comput. Mater. Sci.* **1996**, *6*, 15–50.

[81] J. P. Perdew, K. Burke, M. Ernzerhof, *Phys. Rev. Lett.* **1996**, *77*, 3865–3868.

[82] a) E. Sanville, S. D. Kenny, R. Smith, G. Henkelman, *J. Comput. Chem.* **2007**, *28*, 899–908; b) G. Henkelman, A. Arnaldsson, H. Jónsson, *Comput. Mater. Sci.* **2006**, *36*, 354–360; c) W. Tang, E. Sanville, G. Henkelman, *J. Phys. Condens. Matter* **2009**, *21*, 084204.

[83] O. K. Andersen, R. W. Tank, O. Jepsen in *TB-LMTO-ASA v. 4.7, Vol.* Max-Planck-Institut für Festkörperforschung Stuttgart, **1998**.

[84] D. D. Koelling, B. N. Harmon, *J. Phys. C* **1977**, *10*, 3107.

[85] W. R. L. Lambrecht, O. K. Andersen, *Phys. Rev. B* **1986**, *34*, 2439–2449.